ACS OMEGA

http://pubs.acs.org/journal/acsodf

Article

# Effect of Zn Doping on Structural/Microstructural, Surface Topography, and Dielectric Properties of $Bi_2Fe_4O_9$ Polycrystalline Nanomaterials

Ram Raseele Awasthi,* Sanjeev Kumar Trivedi, Vishal Singh Chandel, Mohammad Shariq, Hussain J. Alathlawi, and Satyendra Pratap Singh

Cite This: *ACS Omega* 2023, 8, 15960−15967

Read Online

ACCESS | Metrics & More | Article Recommendations

**ABSTRACT:** In the present research work, bismuth ferrite mullite type $Bi_2Fe_{4-x}Zn_xO_9$ ($0.0 \leq x \leq 0.05$) nanostructures are prepared by a chemical coprecipitation method and the effect of Zn doping concentration on the structural, surface topography, and dielectric properties is reported. The powder X-ray diffraction pattern of the $Bi_2Fe_{4-x}Zn_xO_9$ ($0.0 \leq x \leq 0.05$) nanomaterial shows an orthorhombic crystal structure. Using Scherer's formula, the crystallite sizes of the nanomaterial $Bi_2Fe_{4-x}Zn_xO_9$ ($0.0 \leq x \leq 0.05$) have been calculated and found to be 23.54 and 45.65 nm, respectively. The results of the atomic force microscopy (AFM) investigations show that spherical shape nanoparticles have grown and are densely packed around each other. AFM/scanning electron microscopy images, however, also illustrate that spherical nanoparticles transform into nanorod-like nanostructures with an increase in Zn concentrations. The transmission electron micrography images of $Bi_2Fe_{4-x}Zn_xO_9$ ($x = 0.05$) showed elongated/spherical shape grains homogeneously distributed throughout the inside of the surface of the sample. The dielectric constants of $Bi_2Fe_{4-x}Zn_xO_9$ ($0.0 \leq x \leq 0.05$) materials have been calculated and found to be 32.95 and 55.32. It is found that the dielectric properties improve with an increase in the Zn doping concentration, making it a good potential contender for multifunctional modern technological applications.

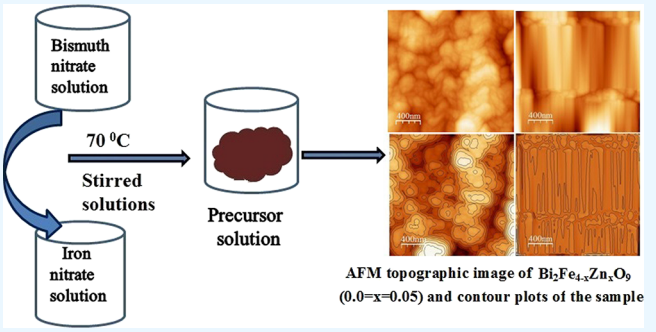


## 1. INTRODUCTION

Over the past few decades, multiferroic materials have been attracting great attention due to coupling of two or three types of ferroic orders, i.e., ferroelectric or antiferroelectric, and ferromagnetic or antiferromagnetic (AF) orders in the same phase.[1−6] Multiferroic materials have tremendous applications in memory storage device, magnetoresistive devices, actuators, solid-state oxide fuels, magnetic recording/memory media, gas sensors, photocatalysts, and their potential utilization of solar energy.[7−15] The current stream of magnetoelectric (ME) effect exists in novel multiferroic materials and is very important due to coupling of electric and magnetic parameters.[16−20] ME multiferroic materials are simultaneously ferromagnetic and ferroelectric, with or without ferroelasticity, having spontaneous magnetization, spontaneous polarization and/or spontaneous deformation reoriented by an applied magnetic field, applied electric field, and/or an applied stress, respectively.[21−28] The ME effect has been taken into advantageous consideration for feasible utilizations in developing a novel category of efficient and operational devices. However, very limited number of single-phase energy-efficient multiferroic materials exist at or above room temperature.[29−36] Among the various multiferroic materials, bismuth-based compounds such as $BiFeO_3$, $BiMnO_3$, and $BiCrO_3$ with a perovskite structure are promising multiferroic materials that show ferroelectric ordering above $T_C$ = 1123 K and a subsequent AF ordering below $T_N$ = 643 K. Mullite-type bismuth ferrite ($Bi_2Fe_4O_9$) is another compound of the bismuth ferrite family (perovskite $BiFeO_3$, mullite $Bi_2Fe_4O_9$, and sillenite $Bi_{25}FeO_{40}$), which exhibits multiferroic properties near room temperature. Thus, $Bi_2Fe_4O_9$ can be regarded as a multiferroic material, which simultaneously shows ferroelectricity with the Curie temperature around 250 K and antiferromagnetism with the Neel temperature around 260 K. These materials have high potential applications in spintronics devices.[37−42] For the past few decades, mullite-type $Bi_2Fe_4O_9$ has attracted wide spread

Received: December 3, 2022
Accepted: April 11, 2023
Published: April 24, 2023

attention due to its fruitful and productive functional properties such as optical, catalytic, electric, magnetic, and gas sensing properties.[39,42−48] Most of the multiferroic materials were noticed at a very low temperature with a significant amount of quality, but dibismuth tetra iron oxide was observed near room temperature, and due to its complex pentagonal symmetric structure and very strong ME coupling, $Bi_2Fe_4O_9$ has been getting great attention. Over the years, $Bi_2Fe_4O_9$ materials with a tunable morphology have been used in extensive applications. The $Bi_2Fe_4O_9$ material shows noncollinear magnetic arrangement with respect to magnetic frustration due to the $Fe^{3+}$ pentagonal lattice. A unit cell of $Bi_2Fe_4O_9$ contains $FeO_4$ tetrahedra and $FeO_6$ octahedra, and in the unit cell Fe ions are uniformly distributed with the Bi ions coordinated by eight oxygen atoms between the tetrahedral and octahedral positions. The unit cell of $Bi_2Fe_4O_9$ includes two sorts of Fe atoms (Fe1 and Fe2), and one of Fe atoms, Fe1, takes up the tetrahedral position enclosed by four oxygen ions ($O^{2-}$) and Fe2 occupies the octahedral position coordinated by six $O^{2-}$ ions. The main limitation of the well-known multiferroic material, $Bi_2Fe_4O_9$, is weak ferromagnetism and poor ferroelectric property at room temperature.[39,44] Most of the studies on $Bi_2Fe_4O_9$ mainly focus on enhancing its magnetic as well as ferroelectric properties, since the material suffers from high current density leakage and high dielectric loss, and negligible magnetization hinders its potential device applications,[39−48] such as electronic information storage, integrated microelectronic memory devices, and spintronics devices. The main aim of the present work is to investigate the effect of Zn doping on physical properties such as dielectric and magnetic properties as well structural/microstructural changes in polycrystalline $Bi_2Fe_4O_9$ materials at room temperature.

## 2. EXPERIMENTAL DETAILS

Presently there are several methods, for example, coprecipitation, solid-state reaction, sol−gel, autocombustion, and hydrothermal methods for the synthesis of bulk polycrystalline nanostructures. In the present paper, mullite type bismuth ferrite ($Bi_2Fe_4O_9$) polycrystalline bulk materials were synthesized by the coprecipitation method. The high-purity chemical reagents of bismuth nitrate pentahydrate ($Bi(NO_3)_3.5H_2O$) and hydrated iron nitrate ($Fe(NO_3)_3.9H_2O$) procured from Merck India private limited were used as raw materials. Mullite type dibismuth tetrairon nonaoxide ($Bi_2Fe_4O_9$) materials have been synthesized by the coprecipitation technique. First, bismuth nitrate and iron nitrate are dissolved in 30 mL of distilled water in an appropriate 1:2 stoichiometric ratio with a constant molarity of 1 M. The resultant precursor solution was continuously stirred for 5 h on a magnetic stirrer until a homogeneous brownish color solution was obtained. Further, the appropriate amount of sodium hydroxide (NaOH) solution was added drop by drop in the precursor solution to get a brownish colored precipitate, and the resultant solution was aged at room temperature for 24 h. Afterward, the suspension solution was filtered and washed several times with distilled water and dried at 200 °C for 6 h in an oven. The resultant dried powder was ground with the help of a mortar and pestle for 8 h to obtain fine particles. In a similar process, Zn doped $Bi_2Fe_{4-x}Zn_xO_9$ ($0.0 \le x \le 0.05$) nanomaterials were also synthesized by doping at a stoichiometric ratio. This prepared powder was calcined from 400 °C for 6 h in order to remove the organic impurities. The calcined powder of $Bi_2Fe_{4-x}Zn_xO_9$ ($0.0 \le x \le 0.05$) materials was ground with the help of a mortar and pestle for 12 h. The above process was repeated three times for better homogeneity and phase purity of powder. The chemical reaction of both $Bi(NO_3)_3.5H_2O$ and $Fe(NO_3)_3.9H_2O$ chemical reagents can be expressed by the following reaction:

$$Bi(NO_3)_3.\ 5H_2O + 2Fe(NO_3)_3.\ 9H_2O \rightarrow Bi_2Fe_4O_9 + (NO_2)\uparrow + (H_2O)\uparrow$$

Finally, the as-calcined fine powders were converted into the form of pellets (thickness of ∼1 mm and diameter ∼3 mm) using a hydraulic press machine at a pressure of 400 kg/cm$^2$, and then, the pellets were sintered at 600 °C for 12 h.

**2.1. Characterization.** The gross structure and phase purity of $Bi_2Fe_{4-x}Zn_xO_9$ ($0.0 \le x \le 0.05$) bulk materials were characterized by a powder X-ray diffractometer [Rigaku, Ultima-IV] with monochromatic CuK$\alpha$ radiation ($\lambda$ = 1.5406 Å). The diffraction data were collected over the diffraction angle ($2\theta$) in the range of 20°−70° with a scanning rate of 0.5°/min and a step size of 0.02°. The surface topography and root mean square (RMS) roughness of pure and 5 wt % Zn doped $Bi_2Fe_4O_9$ bulk materials were obtained by atomic force microscopy (AFM) (Digital Nanomagnetic). The electrical (dielectric) measurements have been carried out as a function of frequency ranging from 100 kHz to 1.5 MHz, using the dielectric set up with a broadband impedance analyzer and an LCR meter.

## 3. RESULTS AND DISCUSSION

**3.1. X-ray Diffraction Analysis.** The representative powder X-ray diffraction (XRD) patterns of the prepared pure and 5 wt % Zn doped $Bi_2Fe_4O_9$ nanomaterials sintered at a temperature of 600 °C are shown in Figure 1. The XRD patterns are perfectly well matched with the prominent peaks in the diffraction pattern, and all assigned diffraction peaks were indexed to various planes of the single phase $Bi_2Fe_4O_9$ nanomaterials using the standard JCPDS no. 80-8638. All the major peaks were well indexed in accordance to the orthorhombic crystal structure with the Pbam space group.

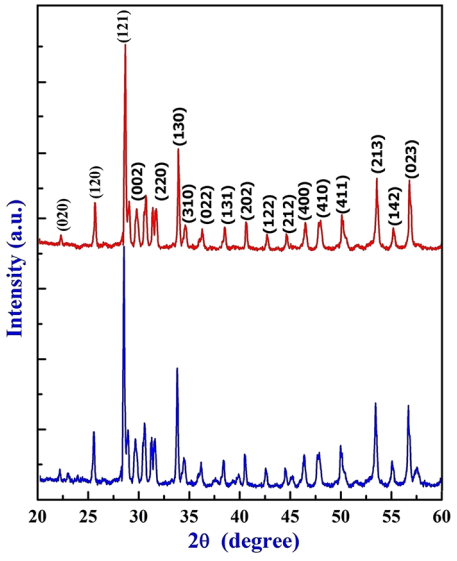


**Figure 1.** XRD patterns of the $Bi_2Fe_{4-x}Zn_xO_9$ ($0.0 \le x \le 0.05$) sample.



https://doi.org/10.1021/acsomega.2c07604
ACS Omega 2023, 8, 15960−15967

The XRD patterns confirm the occurrence of the orthorhombic phase of $Bi_2Fe_4O_9$ nanomaterials with the presence of few impurity phases. After increasing the 5 wt % doping of Zn ions, the diffraction peaks gradually shifting toward the higher angle side may be due to the decrease in the crystallite size of the sample.

By the theoretical approach of Bragg's diffraction law, the diffraction peaks shifting toward the higher angle side decrease the interplaner spacing (d) and consequently reduce the lattice parameters (a,b, and c) as a result of which the crystallite size decreases. On the other hand, with 5 wt % doping of zinc ions, the width of the diffraction peak slightly increases which shows that the crystallite size of $Bi_2Fe_4O_9$ nanomaterials decreases and the peak of impurity phases is suppressed, which reveals the progressive pure structural phase conversion. The interplanar spacing of orthorhombic crystal structures is calculated from the XRD patterns using the Bragg diffraction law ($2d \sin\theta = n\lambda$), and, for orthorhombic structures, the mathematical relation between [$h$ $k$ $l$] and lattice parameters a, b, and c is calculated as given by

$$(1/d) = \sqrt{\left[\frac{h^2}{a^2} + \frac{k^2}{b^2} + \frac{l^2}{c^2}\right]} \quad (1)$$

The lattice parameters of pure and Zn doped $Bi_2Fe_4O_9$ pellets were calculated and found to be $a$ = 7.984 Å, $b$ = 8.475 Å, and $c$ = 5.993 Å. With increasing the Zn doping concentrations from 0 to 5 wt %, the lattice parameters change to $a$ = 7.987 Å, $b$ = 8.497 Å, and $c$ = 5.994 Å. The average crystallite size $D$ of $Bi_2Fe_4O_9$ nanomaterials was calculated by using the Scherrer formula eq 2

$$D = K\lambda/\beta\cos\theta \quad (2)$$

where $K$ is a constant, and for the spherical shape, its value is 0.9, $\lambda$ is the wavelength of powder X-ray, $\beta$ is the full width at half maxima, and $\theta$ is the Bragg diffraction angle. The average crystallite size of pure and 5 wt % Zn doped $Bi_2Fe_4O_9$ nanomaterials was calculated and found to be ~23.54 and ~45.65 nm, respectively. The crystallite size of $Bi_2Fe_4O_9$ nanomaterials decreases with increasing Zn doping concentration. The more precise crystallite size and lattice strain of pure and 5 wt % Zn doped in $Bi_2Fe_4O_9$ nanomaterials have been calculated using Williamson–Hall (W–H) plots. The mathematical relation between the integral full width at half maxima ($\beta$), lattice microstrain ($\varepsilon$), and crystallite size ($D$) is given as follows:

$$\beta\mathrm{Cos}\theta = k\lambda/D + 4\varepsilon\mathrm{Sin}\theta \quad (3)$$

The Bragg diffraction peak width is a combination of the instrumental integral width and the width broadening due to the materials. Therefore, the correct broadening of the diffraction peak of BFO thin films is estimated using the relation

$$\beta = [\beta^2_{\text{measure}} - \beta^2_{\text{instrumental}}]^{1/2} \quad (4)$$

The instrumental integral width ($\beta$-instrumental) was determined from the collected diffraction data of a standard material such as silicon. Furthermore, the linear fit to the data of the graph plotted between $\beta\mathrm{Cos}\theta$ and 4Sin$\theta$ (known as W–H plots), the inverse of intercept gives the value of crystallite size ($D$) and the slope gives the value of the lattice strain ($\varepsilon$). The values of the lattice strain have been calculated from the W-H plots of pure and 5 wt % Zn doped $Bi_2Fe_4O_9$ materials and found to be $2.17 \times 10^{-3}$ and $2.05 \times 10^{-3}$, respectively. Therefore, increasing the doping concentrations decreases the lattice strain. The crystallite sizes are calculated from the Scherrer formula and obtained from the W-H plot; it was found to be close to each other.

**3.2. Atomic Force Micrographs.** Figure 2a–d shows the two-dimensional (2D) AFM, and high-resolution contour plot

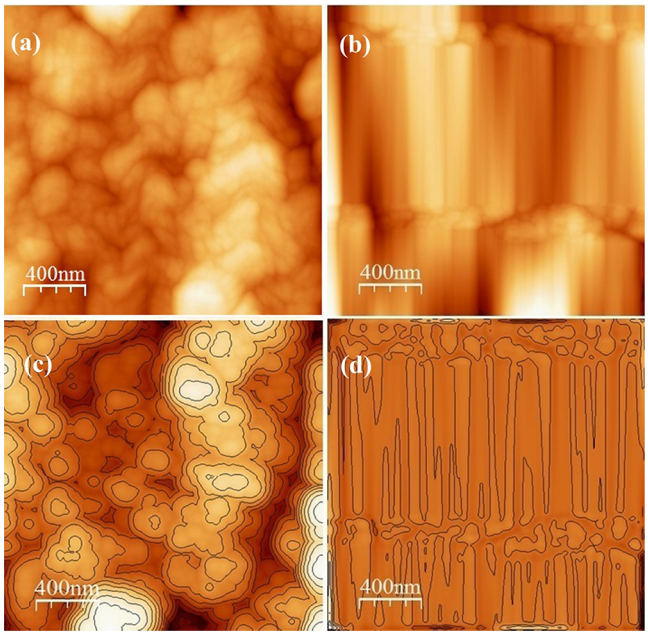


**Figure 2.** (a,b) AFM topographic image of $Bi_2Fe_{4-x}Zn_xO_9$ ($0.0 \le x \le 0.05$) and (c,d) contour image of the sample.

images of $Bi_2Fe_{4-x}Zn_xO_9$ ($0.0 \le x \le 0.05$) sample have been obtained by the chemical coprecipitation method. The AFM micrographs of pure $Bi_2Fe_{4-x}Zn_xO_9$ ($x$ = 0.0) mullite nanomaterials show closely packed spherical shape nanoparticles distributed on the surface. The AFM micrograph also reveals that grains are well linked with each other and consistently distributed throughout the surface of the sample. Furthermore, increasing the Zn-doping concentration from 0 to 5 wt % modified the spherical grains and change into nanorod-like nanostructures shown in Figure 2b. The topographic modification and construction of nanorods may be caused by the large decrement in micro strain with increasing Zn doping concentration. Figure 2c,d shows the contour plots of $Bi_2Fe_{4-x}Zn_xO_9$ ($0.0 \le x \le 0.05$) sample and it clearly reveals the asymmetric grain growth with spherical bases of the nanostructure. However, increasing the Zn doping concentration from 0 to 5 wt % leads to asymmetric grain growth with cylindrical bases.

The RMS roughness and average roughness (AR) of $Bi_2Fe_{4-x}Zn_xO_9$ ($0.0 \le x \le 0.05$) materials examined by WSxM software, were found to be ~26.84, 17.98, and 14.82, 8.65, respectively. The RMS and AR roughness gradually decrease with increasing Zn-doping concentrations, which indicates the modified surface topography of the $Bi_2Fe_{4-x}Zn_xO_9$ ($0.0 \le x \le 0.05$) materials. The particle sizes observed from AFM images (~75 to 90 nm) are larger than the crystallite size calculated from the PXRD data.

The PXRD gives the standard crystallite size of the sample, whereas AFM gives the average particle size (as agglomeration of crystallite/grains). Furthermore the XRD and AFM analysis


https://doi.org/10.1021/acsomega.2c07604
ACS Omega 2023, 8, 15960–15967

confirm that the grain/particle size increases with increasing Zn-doping concentration. The fractal dimension analysis of the $Bi_2Fe_{4-x}Zn_xO_9$ ($0.0 \leq x \leq 0.05$) materials is shown in Figure 3a,b, and the fractal graph, Figure 3c,d, is a manifestation of

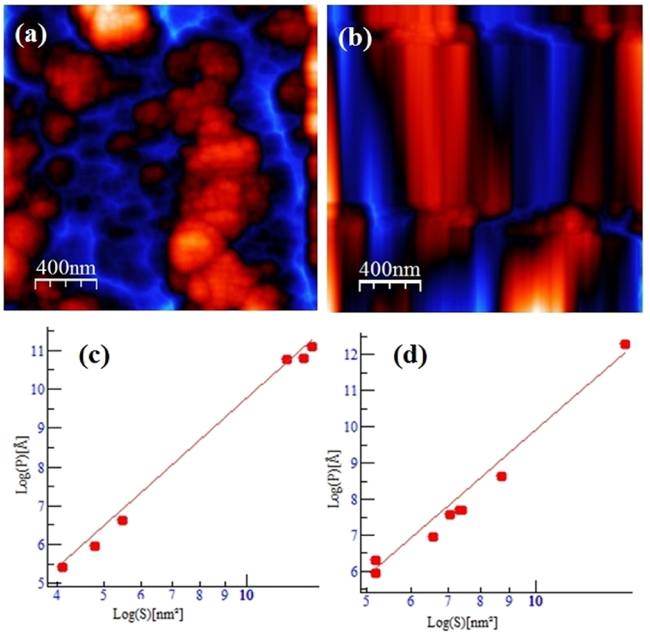


**Figure 3.** (a–d) Fractal dimension analysis of $Bi_2Fe_{4-x}Zn_xO_9$ ($0.0 \leq x \leq 0.05$) nanomaterial surfaces by the power spectrum method.

morphological surfaces. The fractal dimension of pure and Zn doped nanomaterial surfaces is estimated from the slope of a plot of $\log(P)$ versus $\log(S)$. The fractal dimension of $Bi_2Fe_{4-x}Zn_xO_9$ ($0.0 \leq x \leq 0.05$) nanomaterial surfaces is determined by the power spectrum method and found to be 1.292–1.183. Thus, it is evident that the surface roughness decreases with the decrease in the fractal dimension and consequently improves the morphology of the nanomaterial surface. Furthermore, Figure 4a–d shows the three dimensional (3D) AFM topographic image of $Bi_2Fe_{4-x}Zn_xO_9$ ($0.0 \leq x \leq 0.05$) nanomaterials with the irrespective bearing area plot of height profiles.

Increasing the Zn-doping concentration from 0 to 5 wt % modified the granular shape, with a drastic decrement of the *Z*-height distribution, as illustrated in the micrograph. The *Z*-height distributions of the pure and 5 wt % Zn-doped sample were observed from their 3D images and were found to be 19.5 and 0.3 nm. The surface modification and decrement of the *Z*-height distribution as well as RMS roughness may be caused by the decrement of the lattice strain. As seen from the micrographs, the RMS roughness, nanostructure, and *Z*-height distribution are significantly affected and modified by increasing Zn-doping concentrations. The bearing area plot shown in Figure 4c,d indicates that the pure sample has ~52% of surface area within the height range of 19.5 nm. However, with increasing 5 wt % Zn doping concentrations, ~58% of surface area exists within the height range of 0.3 nm which is larger than the height range of the pure sample, which may indicate a decrease in RMS roughness.

**3.3. Magnetic Force Microscopy Analysis.** The magnetic force microscopy (MFM) is one of the most promising tools for the analysis of local magnetic domain and domain wall structure of polycrystalline materials. Figure

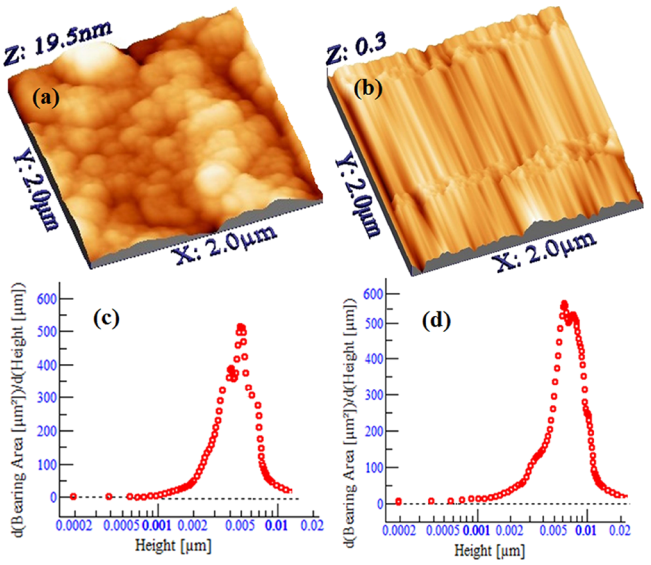


**Figure 4.** (a,b) AFM 3D topographic image of $Bi_2Fe_{4-x}Zn_xO_9$ ($0.0 \leq x \leq 0.05$) and (c,d) bearing area plot of the surface topographic image.

5a,b shows the qualitative MFM phase images of the $Bi_2Fe_{4-x}Zn_xO_9$ ($0.0 \leq x \leq 0.05$) sample, Figure 5c,d shows the contour plot of MFM phase image, and bottom of Figure 5e,f shows the cross-sectional line profile of polycrystalline

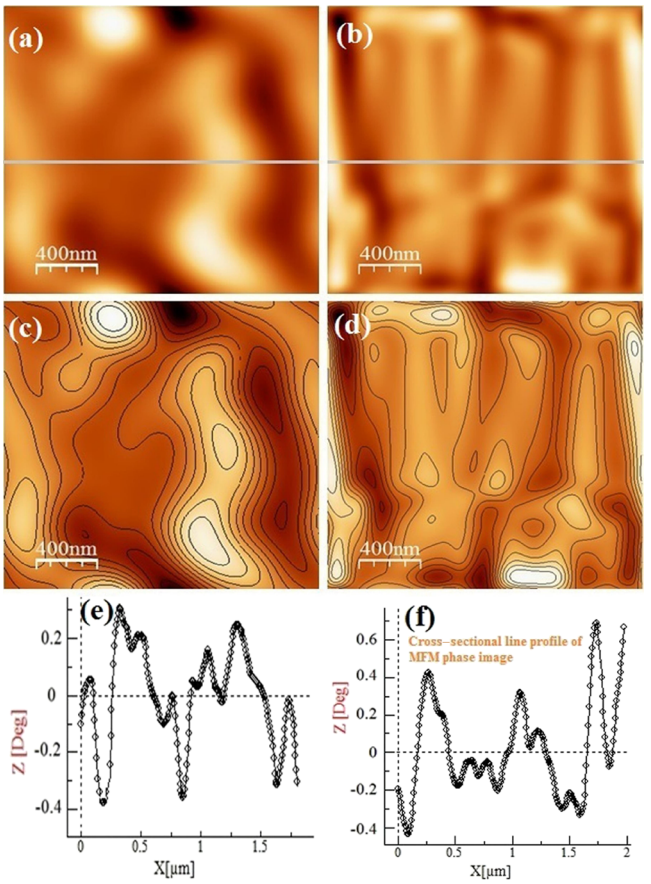


**Figure 5.** (a,b) MFM phase images of $Bi_2Fe_{4-x}Zn_xO_9$ ($0.0 \leq x \leq 0.05$), (c,d) contour plots of the sample sintered, and (e,f) cross-sectional line profile image.



https://doi.org/10.1021/acsomega.2c07604
ACS Omega 2023, 8, 15960–15967

materials. The MFM phase images clearly reveal the presence of irregular nanostructures of the magnetic domains. On the other hand, to determine the orientation of local structure of magnetic domains, contour plots of the MFM phase image of the $Bi_2Fe_{4-x}Zn_xO_9$ ($0.0 \le x \le 0.05$) sample clearly reveal that the asymmetric growth with spherical/elliptical bases of the nanostructure. The cross-sectional line profile images were also recorded for the MFM phase image of the $Bi_2Fe_{4-x}Zn_xO_9$ ($0.0 \le x \le 0.05$) sample. The cross-sectional line profile image of pure $Bi_2Fe_{4-x}Zn_xO_9$ nanomaterials clearly reveals that the phase contrast of polycrystalline materials changes from −0.40° to +0.24° and −0.42° to +0.68°, respectively. The MFM phase images exhibit bright and dark contrast corresponding to specific orientations of the grains along the crystallographic axis corresponding to nucleation of the domain structure clearly visualized in Figure 5e,f.

Figure 5e shows the irregular distribution of magnetic domains on the surface and cross-sectional line profile image of phase contrast change from −0.40° to +0.24° (i.e., total phase difference 0.16°); the magnetic domains provided the magnetic properties of polycrystalline nanomaterials and phase image show the random distribution of magnetic domains. With increasing Zn-doping concentrations from 0 to 5 wt %, cross-sectional line profile image of Figure 5f shows phase contrast change from −0.42° to +0.68° (i.e., total phase difference + 0.26°), and a drastic change in the domain wall dynamic shows improved magnetic properties of polycrystalline materials, which indicates that the there is still tiny phase contrast change observed in the MFM phase image due to the random distribution of magnetic domains and magnetic domains show AF orders. The change of phase contrast observed in MFM phase images, which indicates a change in the orientations of magnetic domains, shows the magnetic properties of the polycrystalline nanomaterials.

**3.4. Scanning Electron Microscopy Analysis.** Figure 6a,b shows the scanning electron microscopy (SEM) micrographs of pure and Zn doped $Bi_2Fe_{4-x}Zn_xO_9$ ($0.0 \le x \le 0.05$) polycrystalline materials.

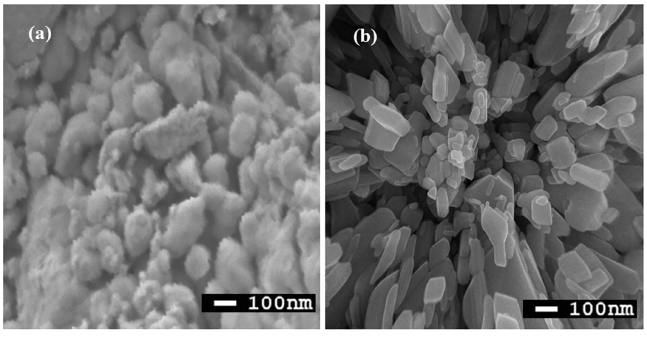


**Figure 6.** (a,b) SEM topographic image of the $Bi_2Fe_{4-x}Zn_xO_9$ ($0.0 \le x \le 0.05$) sample.

The surface morphology of $Bi_2Fe_{4-x}Zn_xO_9$ ($x = 0.00$) materials has a granular structure with average grain size ∼80 nm. However, increasing the Zn doping concentrations in $Bi_2Fe_{4-x}Zn_xO_9$ ($x = 0.00$ to 0.05) materials causes the granular morphology to change into a nanorod-like topographic structure. These surface morphological changes induced by Zn doping might alter the grain growth mechanisms during the nucleation process of $Bi_2Fe_{4-x}Zn_xO_9$ ($0.0 \le x \le 0.05$) polycrystalline materials. It is also observed that the grain size increases from ∼80 to ∼100 nm with increasing Zn doping concentrations.

**3.5. Transmission Electron Microscopy Analysis.** The transmission electron microscopy (TEM) micrographs of $Bi_2Fe_{4-x}Zn_xO_9$ ($x = 0.05$) nanomaterials are shown in Figure 7a. The TEM images of $Bi_2Fe_{4-x}Zn_xO_9$ ($x = 0.05$) showed elongated/spherical shape grains homogeneously distributed throughout inside the surface of the sample.

Figure 7b showing the histogram of the TEM image demonstrates that the $Bi_2Fe_{4-x}Zn_xO_9$ ($x = 0.05$) mean grain size of ∼55 nm is consistently distributed. The observed grain size of $Bi_2Fe_{4-x}Zn_xO_9$ ($x = 0.05$) micrographs using Image J software shows good agreement with the grain size calculated from XRD analysis.

**3.6. Dielectric Analysis.** The dielectric properties of $Bi_2Fe_{4-x}Zn_xO_9$ ($0.0 \le x \le 0.05$) materials have been measured in the frequency range of 20 Hz to 1 MHz at room temperature. To examine the dielectric properties of pure and Zn-doped $Bi_2Fe_{4-x}Zn_xO_9$ polycrystalline materials, complex impedance parameters, capacitance $C_p$, and conductance $G$ were calculated as follows

$$C_0 = \varepsilon_0 \frac{A}{d} \tag{5}$$

$$\varepsilon' = \frac{C_p}{C_0} \tag{6}$$

$$\varepsilon'' = \frac{G}{\omega C_0} \tag{7}$$

Complex dielectric constant

$$\varepsilon^* = \varepsilon' - j\varepsilon'' \tag{8}$$

Tangent loss

$$\tan\delta = \frac{\varepsilon''}{\varepsilon'} \tag{9}$$

where $\varepsilon_0$ is the permittivity of free space or vacuum, $A$ is the area of the sintered pallet, $d$ is the thickness of the pallet, and $\omega = 2\pi f$ is the angular frequency. The variation of dielectric constant ($\varepsilon'$) and tangent loss ($\tan\delta$) as a function of frequency is presented in Figures 8 and 9, respectively. It is observed from Figure 8, the dielectric constant ($\varepsilon'$) decreases with increasing frequency and is almost horizontal in the high frequency range due to dielectric relaxations. The values of dielectric constant ($\varepsilon'$) and tangent loss ($\tan\delta$) of $Bi_2Fe_{4-x}Zn_xO_9$ ($0.0 \le x \le 0.05$) materials have been calculated at a frequency of 1 MHz and found to be 32.95, 55.32 and tangent loss 0.39, 0.78.

It is clearly seen from Figure 8 that the dielectric constant relatively increases from 32.95 to 55.32 with increasing Zn-doping concentration, which confirms it exhibits space charge polarization. It is also observed that tangent loss decreases with increasing Mn-doping concentration can be explained with the help of the Maxwell−Wagner effect. Generally, dipolar, electronic, ionic, and interfacial polarization contributes to the dielectric constant of any material. At low frequencies, the dipolar and interfacial polarizations are effective compared to the dielectric constant. However, at higher frequencies, the electronic polarization is effective and dipolar contribution becomes insignificant. The decrease in dielectric constant with


https://doi.org/10.1021/acsomega.2c07604
ACS Omega 2023, 8, 15960−15967

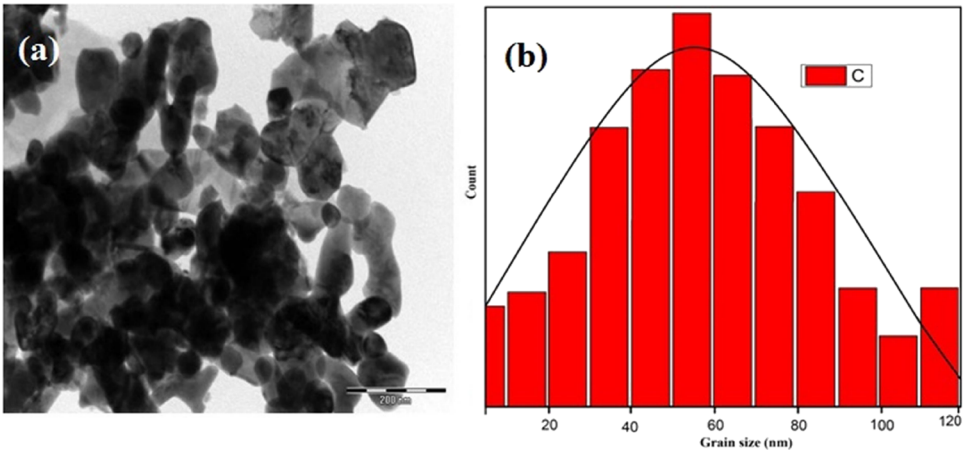


**Figure 7.** (a) TEM image of the $Bi_2Fe_{4-x}Zn_xO_9$ ($x$ = 0.05) sample. (b) Histogram illustrates grain size distribution.

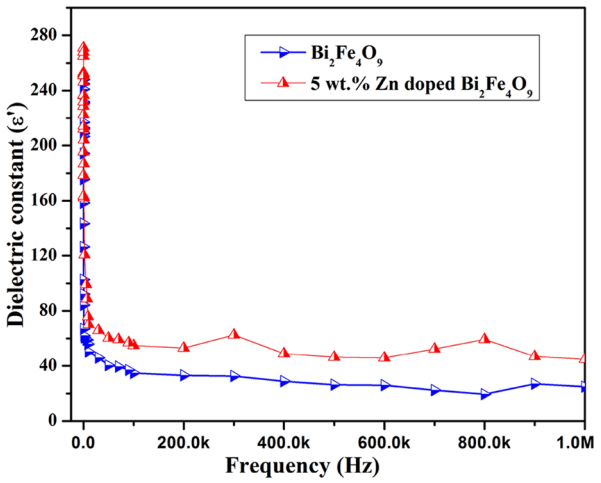


**Figure 8.** Variation of dielectric permittivity ($\varepsilon'$) as a function of frequency of $Bi_2Fe_{4-x}Zn_xO_9$ ($0.0 \leq x \leq 0.05$) nanomaterials.

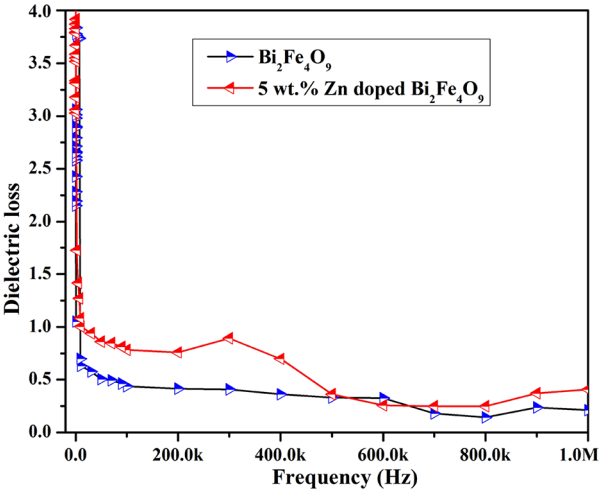


**Figure 9.** Variation of and tangent loss (tan $\delta$) as a function of frequency of $Bi_2Fe_{4-x}Zn_xO_9$ ($0.0 \leq x \leq 0.05$) nanomaterials.

increased frequency could be explained on the basis of the dipole relaxation phenomenon.

It is depicted in Figures 8 and 9, at less frequency, the dipoles in $Bi_2Fe_{4-x}Zn_xO_9$ ($0.0 \leq x \leq 0.05$) polycrystalline materials are able to follow the frequency of the applied field but at higher frequency there is a weak dependence of dielectric constant ($\varepsilon'$) on frequency. After this, the ferroelectric domain contributes to the behavior of the dielectric constant rather than dipole.

## 4. CONCLUSIONS

$Bi_2Fe_{4-x}Zn_xO_9$ ($0.0 \leq x \leq 0.05$) nanomaterials have been successful fabricated through the co-precipitation technique. Further, the structural/microstructural, morphological, and dielectric characterization was carried out using different techniques. The XRD patterns of pure and Zn-doped nanomaterials indicate the formation of the orthorhombic (Pbam) phase. The crystallite size of the $Bi_2Fe_{4-x}Zn_xO_9$ ($0.0 \leq x \leq 0.05$) nanomaterial has been calculated using the Scherrer formula and found to be ~23.54 and ~45.65 nm. The crystallite sizes, lattice parameters, and strain were calculated and found to increase with increasing Zn doping concentration. Surface morphological investigation examined with the help of AFM/SEM micrographs revealed that spherical shape nanoparticles change into nanorod-like nanostructures with increasing Zn doping concentration ($x$ = 0.05). The dielectric properties of $Bi_2Fe_{4-x}Zn_xO_9$ ($0.0 \leq x \leq 0.05$) materials were determined, the dielectric constant was found to be 32.95 and 55.32, and tangent loss was 0.39, 0.78 in the frequency range 20 Hz to 1 MHz. It is found that improved dielectric properties of the $Bi_2Fe_{4-x}Zn_xO_9$ ($0.0 \leq x \leq 0.05$) material make it a promising potential candidate for modern device applications. Future research will focus on the investigation of physical property (ME) and PE measurements of multiferroic properties.

## AUTHOR INFORMATION

### Corresponding Author

**Ram Raseele Awasthi** − *Faculty of Engineering and Technology, Khwaja Muniddin Chisti Language University, Lucknow, Uttar Pradesh 226013, India;* orcid.org/0000-0003-4156-2395; Email: rrawasthi1947@gmail.com

### Authors

**Sanjeev Kumar Trivedi** − *Faculty of Engineering and Technology, Khwaja Muniddin Chisti Language University, Lucknow, Uttar Pradesh 226013, India*

**Vishal Singh Chandel** − *Department of Applied Science and Humanities, Rajkiya Engineering College, Ambedkar Nagar, Uttar Pradesh 224122, India*



https://doi.org/10.1021/acsomega.2c07604
ACS Omega 2023, 8, 15960−15967

**Mohammad Shariq** − *Department of Physics, Jazan University, Jazan 45142, Saudi Arabia*
**Hussain J. Alathlawi** − *Department of Physics, Jazan University, Jazan 45142, Saudi Arabia*
**Satyendra Pratap Singh** − *Department of Physics, AIAS, Amity University, Noida, Uttar Pradesh 201301, India*

Complete contact information is available at: https://pubs.acs.org/10.1021/acsomega.2c07604

### Notes

The authors declare no competing financial interest.

## ■ ACKNOWLEDGMENTS

We are very much thankful to Prof. N. B. Singh, Khwaja Muniddin Chisti Language University Lucknow, 226013, India and Centre for advanced studies, Dr. A.P.J. Abdul Kalam Technical University, Lucknow, India and Department of Physics, University of Lucknow for providing characterization facilities.

## ■ REFERENCES

(1) Ramesh, R. Emerging routes to multiferroics. *Nature* **2009**, *461*, 1218−1219.
(2) Eerenstein, W.; Mathur, N. D.; Scott, J. F. Multiferroic and magnetoelectric materials. *Nature* **2006**, *442*, 759−765.
(3) Fiebig, M.; Lottermoser, T.; Frohlich, D.; Goltsev, A. V.; Pisarev, R. V. Observation of coupled magnetic and electric domains. *Nature* **2002**, *419*, 818−820.
(4) Hill, N. A. Why are there so few magnetic ferroelectrics. *J. Phys. Chem. B* **2000**, *104*, 6694.
(5) Ramesh, R.; Spaldin, N. A. Multiferroics: Progress & Prospects in thin films. *Nat. Mater.* **2007**, *6*, 21−29.
(6) Pooladi, M.; Shokrollahi, H.; Lavasani, S. A. N. H.; Yang, H. Investigation of the structural, magnetic and dielectric properties of Mn-doped $Bi_2Fe_4O_9$ produced by reverse chemical co-precipitation. *Mater. Chem. Phys.* **2019**, *229*, 39−48.
(7) Scott, J. F. Data Storage: Multiferroic Memories. *Nat. Mater.* **2007**, *6*, 256−257.
(8) Sharma, S.; Singh, V.; Kotnala, R. K.; Dwivedi, R. K. Comparative studies of pure $BiFeO_3$ prepared by sol-gel versus conventional solid-state-reaction method. *J. Mater. Sci.* **2014**, *25*, 1915−1921.
(9) Catalon, G.; Scott, J. F. Physics and applications of bismuth Ferrite. *Adv. Mater.* **2009**, *21*, 2463−2485.
(10) Haumont, R.; Kornev, I. A.; Lisenkov, S.; Bellaiche, L.; Kreisal, J.; Dkhil, B. Phase stability and structural temperature dependence in powdered multiferroic BiFeO3. *Phys. Rev. B* **2008**, *78*, No. 134108.
(11) Lawes, G.; Srinivasan, G. Introduction to magnetoelectric coupling and multiferroic films. *J. Phys. D: Appl. Phys.* **2011**, *44*, 243001−243022.
(12) Park, T.-J.; Papaefthymiou, G. C.; Viescas, A. J.; Moodenbaugh, A. R.; Wong, S. S. Size dependent magnetic properties of single crystalline multiferroic $BiFeO_3$ nanaoparticles. *Nano Lett.* **2007**, *7*, 766−772.
(13) Seshadri, R.; Hill, N. A. Visualizing the role of Bi 6s lone pairs in the off center distortion in ferromagnetic $BiMnO_3$. *Chem. Mater.* **2001**, *13*, 2892−2899.
(14) Suresh, P.; Srinath, S. Effect of La substitution on structure and magnetic properties of sol-gel prepared $BiFeO_3$. *J. Appl. Phys.* **2013**, *113*, 17D920.
(15) Xu, J. H.; Ke, H.; Jia, D. C.; Wang, W.; Zhou, Y. Low-temperature synthesis of $BiFeO_3$ nanopowders via a sol−gel method. *J. Alloys Compd.* **2009**, *472*, 473−477.
(16) Wang, Y.; Xu, G.; Ren, Z.; Wei, X.; Weng, W.; Du, P.; Shen, G.; Han, G. Low temperature polymer assisted hydrothermal synthesis of bismuth ferrite nanoparticles. *Ceram. Int.* **2008**, *34*, 1569−1571.
(17) Selbach, S. M.; Einarsrud, M. A.; Tybell, T.; Grande, T. Synthesis of $BiFeO_3$ by wet chemical methods. *J. Am. Ceram. Soc.* **2007**, *90*, 3430−3434.
(18) Singh, A. K.; Kaushik, S. D.; Kumar, B.; Mishra, P. K.; Venimadhav, A.; Siruguri, V.; Patnaik, S. Substantial magnetoelectric coupling near room temperature in $Bi_2Fe_4O_9$. *App. Phys. Lett.* **2008**, *92*, 132910−132913.
(19) Cushing, B. L.; Kolesnichenko, V. L.; Connor, C. J. O. Recent advances in the liquid phase synthesis of inorganic nanoparticles. *Chem. Rev.* **2004**, *104*, 3893−3946.
(20) Jiang, Q. H.; Nan, C. W. Synthesis and properties of multiferroic La-modified $BiFeO_3$ ceramics. *J. Am. Ceram. Soc.* **2006**, *89*, 2123−2127.
(21) Yang, X.; Zhang, Y.; Gang, X.; Wei, X.; Ren, Z.; Shen, G.; Han, G. Phase and morphology evolution of bismuth ferrites via hydrothermal reaction route. *Mater. Res. Bull.* **2013**, *48*, 1694−1699.
(22) Iliev, M. N.; Litvinchuk, A. P.; Hadjiev, V. G.; Gospodinov, M. M.; Skumryev, V.; Ressouche, E. Phonon and magnon scattering of antiferromagnetic $Bi_2Fe_4O_9$. *Phys. Rev. B* **2010**, *81*, 024302−0243028.
(23) Sagdeo, A.; Mondal, P.; Upadhyay, A.; Sinha, A. K.; Srivastava, A. K.; Gupta, S. M.; Chowdhury, P.; Ganguli, T.; Deb, S. K. Correlation of microstructural and physical properties in bulk BiFeO3 prepared by rapid liquid-phase sintering. *Solid State Sci.* **2013**, *18*, 1−9.
(24) Jing, C.; Junling, W.; Haiyang, D.; Tao, L.; Zhenping, C. Investigations on the structure, defects, electrical and magnetic properties of Ni-substituted $BiFeO_3$ ceramics. *J. Mater. Sci.: Mater. Electron.* **2016**, *27*, 11151−11157.
(25) Khan, U.; Adeela, N.; Javed, K.; Riaz, S.; Ali, H.; Iqbal, M.; Han, X. F.; Naseem, S. Influence of cobalt doping on structural and magnetic properties of $BiFeO_3$ nanoparticles. *J. Nanopart. Res.* **2015**, *17*, 429.
(26) Ruan, Q. J.; Zhang, W. D. Tunable morphology of $Bi_2Fe_4O_9$ crystals for photocatalytic oxidation. *J. Phys. Chem. C* **2009**, *113*, 4168−4173.
(27) Raghavender, A. T.; Hong, N. H. Effects of Mn doping on structural and magnetic properties of multiferroic $BiFeO_3$ nano grains made by sol-gel method. *J. Magn.* **2011**, *16*, 19−22.
(28) Chauhan, S.; Kumar, M.; Chhoker, S.; Katyal, S. C.; Singh, H.; Jewariya, M.; Yadav, K. L. Multiferroic magnetoelectric and optical properties of Mn doped $BiFeO_3$ nanoparticles. *Solid State Commun.* **2012**, *152*, 525−529.
(29) Singh, S. K.; Ishiwara, H.; Sato, K.; Maruyama, K. Microstructure and frequency dependent electrical properties of Mn-substituted $BiFeO_3$ thin films. *J. Appl. Phys.* **2007**, *102*, No. 094109.
(30) Zhang, M.; Yang, H.; Xian, T.; Wei, Z. Q.; Jiang, J. L.; Feng, Y. C.; Liu, X. Q. Polyacrylamide gel synthesis and photocatalytic performance of $Bi_2Fe_4O_9$ nanoparticles. *J. Alloy Compd.* **2011**, *509*, 809−812.
(31) Rao, T. D.; Karthik, T.; Asthana, S. Investigation of structural, magnetic and optical properties of rare earth substituted bismuth ferrite. *J. Rare Earth* **2013**, *31*, 370.
(32) Yang, Z.; Huang, Y.; Dong, B.; Li, H. L.; Shi, S. Q. Densely packed single-crystal $Bi_2Fe_4O_9$ nanowires fabricated from a template-induced sol-gel route. *J. Solid State Chem.* **2006**, *179*, 3324−3329.
(33) Park, T.; Papaefthymiou, G. C.; Moodenbaugh, A. R.; Mao, Y.; Wong, S. S. Synthesis and characterization of submicron single-crystalline $Bi_2Fe_4O_9$ Cubes. *J. Mater. Chem.* **2005**, *15*, 2099−2105.
(34) Kumar, A.; Varshney, D. Crystal structure refinement of $Bi_{1-x}Nd_xFeO_3$ multiferroic by the Rietveld method. *Ceram. Int.* **2012**, *38*, 3935−3942.
(35) Shamir, N.; Gurewitz, E.; Shaked, H. The magnetic structure of $Bi_2Fe_4O_9$-Analysis of neutron diffraction measurements. *Acta Cryst. A* **1978**, *34*, 662−666.
(36) Das, R.; Mandal, K. Magnetic, ferroelectric and magnetoelectric properties of Ba-doped $BiFeO_3$. *J. Magn. Magn. Mater.* **2012**, *324*, 1913.
(37) Liu, T.; Xu, Y.; Zeng, C. Synthesis of $Bi_2Fe_4O_9$ via PVA sol-gel route. *Mater. Sci. Eng., B* **2011**, *176*, 535−539.

(38) Zhao, J.; Liu, T.; Xu, Y.; He, Y.; Chen, W. Synthesis and characterization of $Bi_2Fe_4O_9$ powders. *Mater. Chem. Phys.* **2011**, *128*, 388−391.
(39) Varshney, D.; Kumar, A.; Verma, K. Effect of A site and B site doping on structural, thermal, and dielectric properties of $BiFeO_3$ ceramics. *J. Alloys Compd.* **2011**, *509*, 8421−8426.
(40) Rout, J.; Choudhary, R. N. P. Structural transformation and multiferroics properties of Ba-Mn co-doped $BiFeO_3$. *Phys. Lett. A* **2016**, *380*, 288−292.
(41) Rana, K.; Thakur, P.; Thakur, A.; Tomar, M.; Gupta, V.; Mattei, J. L.; Queffelec, P. Influence of samarium doping on magnetic and structural properties of M-type Ba-Co hexaferrite. *Ceram. Int.* **2016**, *42*, 8413−8418.
(42) Basith, M. A.; Khan, F. A.; Ahmmad, B.; Kubota, S.; Hirose, F.; Ngo, D. T.; Tran, Q. H.; Molhave, K. Tunable exchange bias effect in magnetic $Bi_{0.9}Gd_{0.1}Fe_{0.9}Ti_{0.1}O_3$ nanoparticles at temperatures up to 250 K. *J. Appl. Phys.* **2015**, *118*, No. 023901.
(43) Wodecka-Dus, B.; Dzik, J.; Bernard, H.; Osinska, K.; Lisinska-Czekaj, A.; Czekaj, D. Application of impedance spectroscopy for $Bi_{1-x}Nd_xFeO_3$ ceramics characterization. *Mater. Sci. Forum* **2013**, *71*, 730−732.
(44) Hussain, T.; Siddiqi, S. A.; Atiq, S.; Awan, M. S. Induced modifications in the properties of Sr doped $BiFeO_3$ multiferroics. *Prog. Nat. Sci.: Mater. Int.* **2013**, *23*, 487−492.
(45) Dhanalakshmi, B.; Pratap, K.; Rao, B. P.; Rao, P. S. V. S. Effects of Mn doping on structural, dielectric and multiferroic properties of $BiFeO_3$ nanoceramics. *J. Alloys Compd.* **2016**, *676*, 193−201.
(46) Du, Y.; Cheng, Z. X.; Shahbazi, M.; Collings, E. W.; Dou, S. X.; Wang, X. L. Enhancement of ferromagnetic and dielectric properties in lanthanum doped $BiFeO_3$ by hydrothermal synthesis. *J. Alloys Compd.* **2010**, *490*, 637−641.
(47) Deng, H.; Zhang, M.; Hu, Z.; Xie, Q.; Zhong, Q.; Wei, J.; Yan, H. Enhanced dielectric and ferroelectric properties of Ba and Ti co-doped $BiFeO_3$ multiferroic ceramics. *J. Alloys Compd.* **2014**, *582*, 273−276.
(48) Srivastava, A.; Singh, H. K.; Awana, V. P. S.; Srivastava, O. N. Enhancement in magnetic and dielectric properties of La and Pr co substituted $BiFeO_3$. *J. Alloys Compd.* **2013**, *552*, 336−344.



https://doi.org/10.1021/acsomega.2c07604
*ACS Omega* 2023, 8, 15960−15967